Journal Pre-proofs

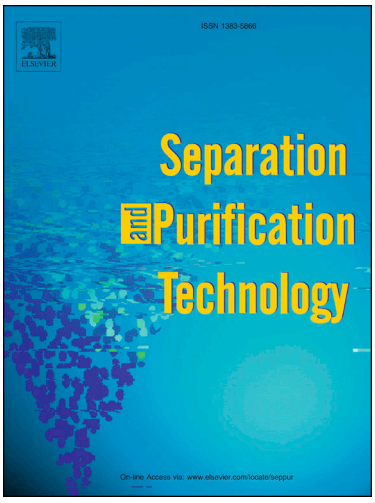

Breaking through the selectivity-permeability tradeOFF using nano zeolite-Y for micellar enhanced ultrafiltration dye rejection application

Shaheen Fatima Anis, Boor Singh Lalia, Raed Hashaikeh, Nidal Hilal

PII: S1383-5866(20)30428-7
DOI: https://doi.org/10.1016/j.seppur.2020.116824
Reference: SEPPUR 116824

To appear in: *Separation and Purification Technology*

Received Date: 26 January 2020
Revised Date: 4 March 2020
Accepted Date: 7 March 2020

Please cite this article as: S. Fatima Anis, B. Singh Lalia, R. Hashaikeh, N. Hilal, Breaking through the selectivity-permeability tradeOFF using nano zeolite-Y for micellar enhanced ultrafiltration dye rejection application, *Separation and Purification Technology* (2020), doi: https://doi.org/10.1016/j.seppur.2020.116824

BREAKING THROUGH THE SELECTIVITY-PERMEABILITY TRADEOFF USING NANO ZEOLITE-Y FOR MICELLAR ENHANCED ULTRAFILTRATION DYE REJECTION APPLICATION

Shaheen Fatima Anis[a], Boor Singh Lalia[a], Raed Hashaikeh[a*], Nidal Hilal[a, b*]

[a] NYUAD Water Research Center. New York University Abu Dhabi, P.O. Box 129188, Abu Dhabi, United Arab Emirates

[b] Centre for Water Advanced Technologies and Environmental Research (CWATER), College of Engineering, Swansea University, Fabian Way, Swansea SA1 8EN, United Kingdom

[a,b*]Corresponding author: Centre for Water Advanced Technologies and Environmental Research (CWATER), College of Engineering, Swansea University, Fabian Way, Swansea SA1 8EN, United Kingdom. Email: n.hilal@swansea.ac.uk. Tel: +971-6284000

[a*] Corresponding author: NYUAD Water Research Center. New York University Abu Dhabi, P.O. Box 129188, Abu Dhabi, United Arab Emirates. Email: raed.hashaikeh@nyu.edu Tel: +971 2 6284626

Abstract

Membrane performance is a region of growing research interest, where new functional nanomaterials are continually sought. In this study, nano zeolite type Y was prepared through a unique ball milling process. The produced zeolite has a high surface area, and abundant flow channels with a well-defined pore structure facilitating water passage, but at the same time restricting the passage of contaminants through the molecular sieving effect. Polysulfone (PSf) membranes were prepared through phase inversion with nano-Y loadings from 0.2 to 1.5 wt. %. Membranes were characterized for their structure, morphology, thermal stability and porosity. The developed membranes were tested for micellar enhanced ultrafiltration (MEUF) cationic dye rejections. The addition of nano-Y zeolite affected both the flux and dye rejection of the membranes. Optimum performance was obtained at 0.4 wt. % nano-Y loading, giving a rejection of 99.5% and a corresponding flux of 105 $L.m^{-2}.h^{-1}$. The static contact angle measurements indicate that membrane hydrophilicity increased with progressive nano-Y additions until 0.4 wt. %, after which the membrane showed no further change in hydrophilic character. The obtained effects of nano-Y addition on membrane performance was attributed to the well-connected 3-D microporous structure in which nano-Y zeolite provided preferential water pathways though nanoporous hydrophilic channels. Whereas, the high dye rejection was attributed to the fact that nano-Y zeolite is negatively charged and, as a result, provided resistance to the negatively charged micelles, and further restricted its passage through the microporous zeolite structure.

Keywords: Ultrafiltration; micellar; nano-zeolite; dye rejection; phase inversion

1. INTRODUCTION

Membrane based, pressure driven filtration processes are important tools for water treatment [1]. UF is one such process in which membranes have pore diameters ranging from about 0.1 µm to 0.01 µm. This makes the process attractive for removing a range of viruses, dyes, large proteins, and other several industrial contaminants for wastewater treatment. Micellar-enhanced ultrafiltration (MEUF) is one such UF technology which utilizes a surfactant-based separation technique to remove industrial contaminants such as ions, organics, dyes and other pollutants [2]. MEUF allows the rejection of low molecular weight contaminants to be rejected by an ultrafiltration membrane through molecular weight enlargement using surfactants. Surfactants are amphiphilic molecules which consist of a hydrophilic head and a hydrophobic chain. The dissolved contaminant can get trapped by the surfactant micelles through charge attraction and thus solubilize in in the micelle interior. This increases the hydrodynamic size of the contaminant which can then be easily rejected by the membrane. MEUF provides an advantage over NF and conventional UF, where membranes with larger pore diameter can reject low molecular weight contaminants with less pressure and energy requirements. In addition, MEUF is known to reject molecules even at lower concentrations as the solute can bind to the surfactant owing to ionic interactions. The technique finds great potential in the removal of organic dyes from colored effluent. The environmental effects are dominated by the liquid waste produced by textile, paper and plastic industries [3], where pretreatment of rejected streams becomes essential before discharging them into the sea.

Many of the existing UF membrane materials are limited with their inherent properties rendering low selectivity and permeability for these membranes [4]. Thus, membrane modification has emerged as a topic of great research interest [5], whereby many of the existing UF membrane materials such as polysulfone (PSf) and Polyvinylidene fluoride (PVDF) have been modified either by incorporating hydrophilic polymers [6] or through functional nanomaterials [7, 8]. With nanotechnology development, several functional nanomaterials have emerged for this application including alumina [9], silica [10], zinc oxide [11], titanium dioxide [12] and zeolites [13]. These have been reported to improve membrane hydrophilicity [14], thermal stability [15], and antifouling properties [4]. Nevertheless, limitations arise when either the selectivity or membrane permeability have to be compromised. A tradeoff between the two is often encountered. Zeolites represent one such class of materials which hold immense potential in breaking this tradeoff.

Zeolites are crystalline aluminosilicates which have a well-defined inorganic structure [16]. The channels and pores act as molecular sieves, hence rendering it attractive for rejection of several species through the size exclusion principle. In addition, the negative charge associated with the alumina makes it favorable for absorbing ions with opposite charge. Majority of the reported studies for UF membrane utilize nano-zeolite with a low Si/Al ratio [4, 13]. Han et al. [13] reported zeolite NaA/ poly (phthalazinone ether sulfone ketone) composite UF membranes prepared through the phase inversion process, for the removal of Titan Yellow dye solution. A 3 wt.% NaA content gave the optimum membrane performance, with improved hydrophilicity, water permeability, antifouling property and enhanced dye rejections. A higher content caused nanoparticle agglomeration as concluded from their microscopic studies. Yilmaz Yurekli [14] impregnated zeolite NaX (from 1 to 10 wt.%) into PSf membranes through the phase inversion

technique for heavy metal removal from wastewater. They reported an initial decrease in membrane contact angle from 69^{o} to 67^{o} with zeolite loadings from 1-5 wt.%. However, an increase in contact angle >80 ^{o} was recorded for higher NaX additions of 10 wt. %, due to surface void formations. The performance of the hybrid membrane was determined under dynamic conditions, which gave better rejections for lead, compared to smaller metallic ions such as nickel. Nevertheless, the low Si/Al ratio is reported to have more defects in the form of grain boundaries compared to high Si/Al ratio zeolites, resulting in low selectivity [17]. Several other studies report the usage of low Si/Al ratio zeolites for UF membranes [4, 18, 19]. However, high-silica zeolites have been found to be more effective for removing organic pollutants from various industrial wastes [20]. In addition, the high Si/Al ratio influences the silanol (Si-OH) groups which can adsorb water by forming stable adducts [20].

Faujasite (FAU) type zeolite such as zeolite-Y has been reported to be a potential candidate for many membrane based applications [21, 22]. It possesses inter-crystalline pores which form a 3-D channel system facilitating preferential water pathways. FAU structure has a high pore volume, 12-memberd ring structure, hence, even with a high Si/Al ratio, it shows favorable water transport properties compared to other zeolite structures which have similar Si/Al molar ratios [20] . Direct production of zeolite-Y with a high Si/Al ratio is restricted due to unfavorable hydrothermal synthesis route [23]. Following this limitation, Bota el al. [23] reported the production of zeolite-Y nanoparticles (nano-Y) from commercial micron sized particles through the ball milling approach. Ball milling processing parameters were optimized for producing highly crystalline nano-Y particles which showed promising performances in various applications [24, 25]. Recently, our group reported the use of nano-Y for desalination, where incorporation of

nano-Y in reverse osmosis membranes resulted in increased flux and salt rejections compared to other zeolite type such as zeolite-LTL [26]. In the present study, we assess embedding nano-Y in PSf UF membranes and the resulting performance for MEUF dye rejection. Nano-Y, due to its 3-D structure and well-ordered microporous channels seems a promising for such an application where high flux is desirable. In addition, the highly negative charge of the nano-Y can contribute towards better rejection of the dye molecules. Thus, this work aims to study the effect of nano-Y on UF membranes for improved performances.

2. EXPERIMENTAL

2.1 Materials

The following chemicals were purchased from Sigma Aldrich: polyvinylpyrrolidone (PVP) (M_w =135,000 g.mol^{-1}), PSf pellets (M_w=35,000 g.mol^{-1}), n-Methyl-2-Pyrrolidone (NMP), ethanol, methanol, surfactant sodium dodecylbenzenesulfonate (SDS) (M_w=348.48 g.mol^{-1}), and crystal violet dye (CVD) in the powder form (M_w=407.98 g.mol^{-1}). Zeolite-Y (CBV 720) was purchased from Zeolyst International, while carbon nanostructures (CNS) were obtained from Applied Nanostructured solutions LLC.

Zeolite nano-Y was obtained by ball milling using an E-max high energy ball mill machine from Retsch, Germany using the method reported in [23]. In brief, micron-Y zeolite, obtained from zeolyst was used along with CNS in the weight ratio of 3:1 respectively, while the solvents ethanol and deionized water (DI) ratio was kept as 1:1. They were grinded in zirconia jars using zirconia balls of 2 mm diameter. Ball milling was carried out at 1000 rpm for 1 h, after which the samples

were centrifuged (Multifuge X3R, Thermo Scientific) at 4000 rpm for 10 min. This enabled separation of nano-Y from the solvents. The bottom part was collected as detailed in [23]. The nano-Y/CNS mixture was then dried at 80 °C overnight, following calcination at 610 °C for 5 h (Nabertherm 400-1 series furnace).

2.2 Nano zeolite/PSf membrane preparation

UF membranes were fabricated via the wet phase-inversion method [27]. A semi-automatic casting machine (PMI Porous Materials Inc. Model BT FS- TC) was used for this purpose. The polymer dope solution was cast on a glass plate using a constant shear rate of 200 s^{-1}, with a casting blade thickness kept constant at 150 µm. After casting, the glass plate was immediately transferred to a DI water bath at room temperature to induce polymer precipitation. The bath water was changed after 1h, and the membranes were left in the new DI water bath for 24 h. Subsequently, the membranes were immersed in methanol for about 6 h, to ensure complete removal of the excess solvent. They were then stored in DI water until further testing.

For the polymer dope solution, PVP was first allowed to dissolve in NMP at 50 °C. PVP, a water soluble polymer is used in this study as a pore-forming agent which increases membrane porosity, similar to reported in [28, 29]. Following this, PSf was added to the solution, which was magnetically stirred overnight at 50 °C. Figure 1 shows the membrane preparation steps through a schematic. The effect of nano-Y concentration was studied by varying its concentration from 0.2 wt.% to 1.5 wt.% in the NMP solvent. Nano-Y/PSf membranes were prepared in a similar fashion to PSf membranes, except that nano-Y zeolite nanoparticles were dispersed in NMP using ultrasonication (Q Sonica Ultrasonic Processor) before dissolving PVP in the nano-Y-NMP

dispersion. In all cases, PSf and PVP concentration was fixed at 15 wt.% and 10 wt.% respectively.

Membranes with varying nano-Y concentrations were defined as highlighted in Table 1.

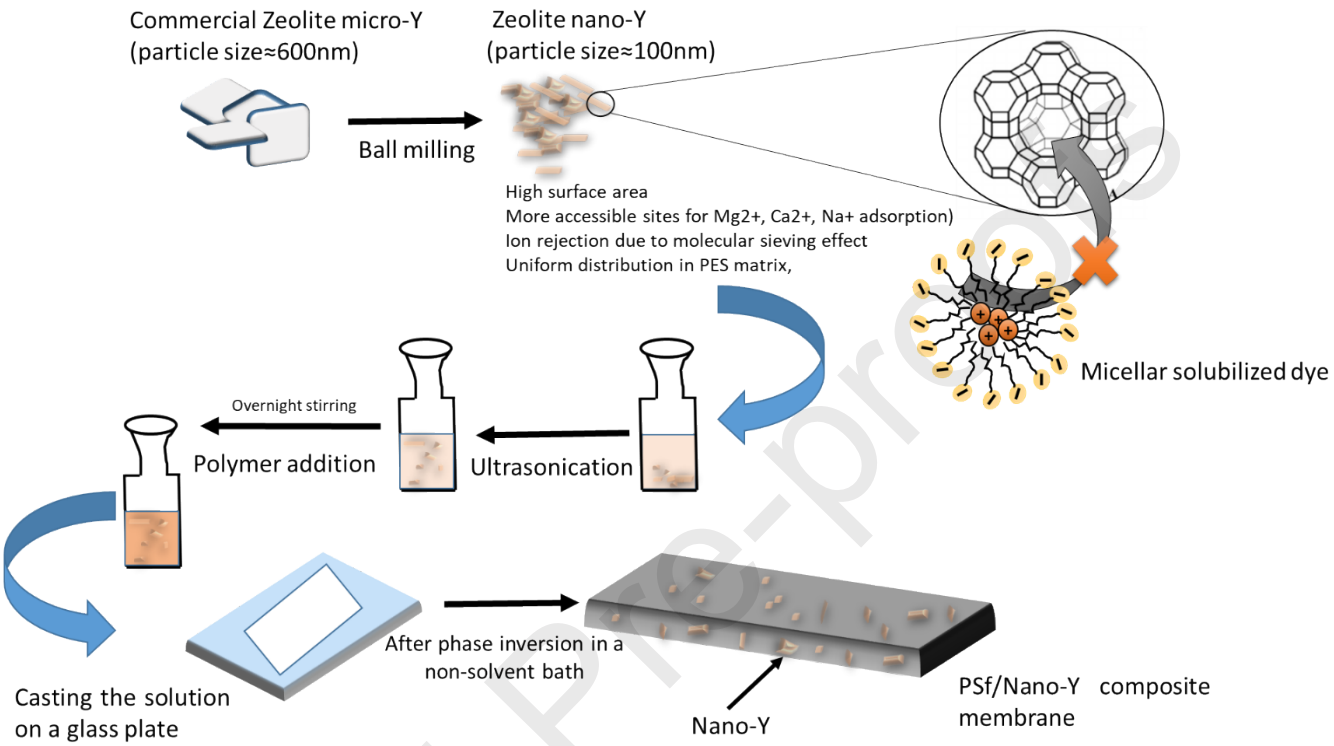

Figure 1: Schematic of membrane preparation

Table 1: Composition of Nano-Y/PSf casting solutions of the membranes from M0 to M1.5

Membrane	PSf (wt. %)	PVP(wt. %)	Nano-Y(wt. %)	NMP (wt. %)	Total (wt. %)
M0	15	10	0	75.0	100
M0.2	15	10	0.2	74.8	100
M0.4	15	10	0.4	74.6	100
M0.6	15	10	0.6	74.4	100
M1.0	15	10	1.0	74.0	100
M1.5	15	10	1.5	73.5	100

2.3 Characterization

Prior to membrane characterization, all membranes were air dried. Structural integrity of zeolite nano-Y and nano-Y/PSf membranes were studied through X-ray diffraction (XRD) (Panalytical Empyrean diffractometer). Ni-filtered CuKα (λ=1.5056 Å) radiations were used, with a voltage of 40 kV and a current of 30 mA in the 2–40° half angle range. Surface chemistry of the membranes were determined by attenuated total reflectance Fourier transform infrared spectroscopy (ATR-FTIR) (iDT ATR- Nicolet iS5 Spectrometer) over the range from 4000-650 cm^{-1}. Before analysis, the samples were air dried followed by vacuum drying over night at 40 °C to remove moisture.

The zeta potential of micro-Y CBV 720 particles and ball milled nano-Y particles was measured by dynamic light scattering (Nano ZS Zetasizer, Malvern Instrument) using a DTS1070 disposable cell. The measurements were carried out using dilute aqueous colloidal suspensions of the particles, 0.01 wt. % in DI water.

Membrane morphology was studied using scanning electron microscopy (SEM) (FEI Quanta 450 FEG) at 10 kV. Before viewing the sample under SEM, all samples were gold coated (108 Auto Sputter Coater, Ted Pella). Membrane composition was qualitatively analyzed using energy dispersive spectroscopy (EDS) integrated with SEM. In order to examine the morphology of zeolite nano-Y, transmission electron microscope (FEI TEM Talos F200X) was used. TEM sample was prepared by dispersing zeolite nanoparticles in ethanol and putting a droplet of that dispersion onto a carbon coated copper grid.

Nano-Y and nano-Y/PSf membrane surface area was determined through Brunauer–Emmett–Teller (BET) analysis (NOVA®4200e Quantachrome Instruments) in a relative pressure of P/P_o = 0.05–0.30, while the pore size distribution was obtained using the Barrett–Joyner–

Halenda (BJH) method. Membrane porosity was measured by using a wetting liquid (Silwick™; surface tension = 22.1 dynes.cm^{-1}) whereby dry and wet (membrane pores filled with silwick) membrane weights were measured following a procedure similar to described in [30]. Three measurements were made and their average was recorded.

Contact angle measurements (Kruss Drop Shape Analyzer-DSA 100) were taken to examine the wettability of the membrane surface to water. 2 µL DI water droplets, with sessile drop technique was utilized. Contact angle was evaluated through an image processing software, *ADVANCE* using the tangent method. Five measurements were taken for each membrane, and an average was calculated in the end.

Thermal characteristics of the membranes were studied through thermogravimetric analysis (TGA) (TG 209 Tarsus, NETZSCH) and differential scanning calorimetry (DSC) (DSC 214 Polyma, NETZSCH). The samples were dried under vacuum at 40 ˚C overnight before the measurements. Sample mass (≈5 mg) was placed in an alumina crucible to study its thermal degradation behavior using TGA at a heating rate of 10 °C.min^{-1} from room temperature to 950 °C under a nitrogen flow of 20 mL/min. Glass transition temperature (T_g) of the membranes was evaluated using DSC whereby a sample of known mass (≈5 mg) was placed in an aluminium pan next to an empty reference pan. The pans were heated under nitrogen flow of 20 mL/min at a rate of 10 °C.min^{-1} from room temperature to 500 °C.

2.4 Ultrafiltration Testing

All filtration experiments were carried out using a laboratory-scale crossflow cell setup (UF system Hydra model, Convergence Inspector). Each time, a fresh membrane (immersed in DI

water) was used and then placed in a filtration cell with an effective area of 40 cm^2. Feed pressure and feed flow rate were controlled and monitored through the software. In all experiments, a constant feed flow of 10 $L.h^{-1}$ was used.

PWF studies for M0 to M1.5 membranes were carried out at constant pressures of 2, 4 and 6 bar. Flux was calculated for a known interval of time using the following equation:

$$J^w = \frac{V(t)}{A} \qquad \text{Equation 1}$$

Where, J_w ($L.m^{-2}.h^{-1}$) is the pure water flux, and V(t) is the volume per hour of permeate collected for 30 min using a membrane of area A (m^2). V(t) was read directly from the software.

In the present study, anionic surfactant, sodium dodecylbenzenesulfonate (SDS), is used for the MEUF experiments. The solution for UF experiments was prepared as follows: SDS was first dissolved in DI water, after which crystal violet dye (CVD) was dissolved at a concentration of 20 $mg.\ L^{-1}$. The concentration of SDS was chosen above its critical micellar concentration (CMC) of 2.78 mM [31] and fixed at 8.2 mM to prepare all the feed solutions. The pH of the solution was determined to be 8.1. Permeate flux was calculated at a trans membrane pressure of 6 bar, using equation 1. After each run, the cell and the tubing were thoroughly flushed with DI water.

The following equation was used to measure CVD rejection:

$$\%\mathbf{R} = \left(\mathbf{1} - \frac{\mathbf{Cp}}{\mathbf{Cf}}\right) \times \mathbf{100} \qquad \text{Equation 2}$$

Where %R is the dye rejection and, C_p and C_f (mg/mL) are the dye concentrations in permeate and feed solutions respectively. Concentration was measured using a spectro-photometer (UV–3100PC, VWR) at wavelength of 582 nm.

Dye antifouling behavior was analyzed by measuring the flux recovery ratio (FRR), using the following equation,

$$\mathbf{FRR} = \left(\frac{\mathbf{Jc}}{\mathbf{Jw}}\right) \times \mathbf{100} \quad \text{Equation 3}$$

Where, J_w and J_c are the initial PWF ($L{\cdot}m^{-2}{\cdot}h^{-1}$) and the PWF after backwashing ($L{\cdot}m^{-2}{\cdot}h^{-1}$) of the membrane respectively.

The fabricated membranes were also tested for CVD dye rejection without the surfactant. Similar dye concentration of 20 mg. L^{-1} was tested at a pressure of 6 bar. Flux and rejection were calculated similar to the method adapted for CVD/SDS experiments.

3. RESULTS AND DISCUSSION

3.1 Zeolite Nano-Y Characterization

Various techniques were used to characterize zeolite nano-Y for its structure, morphology, BET surface area and pore diameter. Figure 2a shows the XRD pattern of zeolite nanoparticles produced through the ball milling approach. All major peaks corresponding to zeolite-Y ($2\theta<20^{\circ}$) were obtained [25]. The characteristic peaks of zeolite-Y obtained at 2θ values of 6.3°, 12.1°, 15.9°, 20.7° and 24.1° corresponding to the respective planes at (111), (311), (331), (440) and (533) confirmed that the ball milling method did not bring about any structural change in the zeolite nanoparticles. The morphology of the nanoparticles as studied through TEM is shown in

Figure 2b. Zeolite nanoparticles can be seen with a somewhat irregular structure due to mechanical grinding, with sizes less than 100 nm. This has also been reported [23, 25], where the same material produced through a ball milling approach produced similar results. Figure 2c shows the N_2 adsorption/desorption curves, while the inset shows the pore size distribution of the zeolite nanoparticles. In particular, nano-Y displays type IV hysteresis loop which is common in mesoporous zeolites [32] possessing a bimodal pore size distribution. Recent studies [33] have detailed on the intracrystalline connectivity between micro- and mesopores in zeolite-Y. The BET surface area was calculated to be 1324 m^2/g, with the micropore diameter of the microporous zeolite centering at 2 nm. The difference in zeta potential for micro and nano-Y is shown in Figure 2d. The more negative zeta potential of nano-Y of -36.6 mV when suspended in DI water implies its stability as a membrane additive. The negative zeta potential can be beneficial in repelling the anionic surfactant, while simultaneously attracting any positively charges insolubilized dye molecules (section 3.7.2).

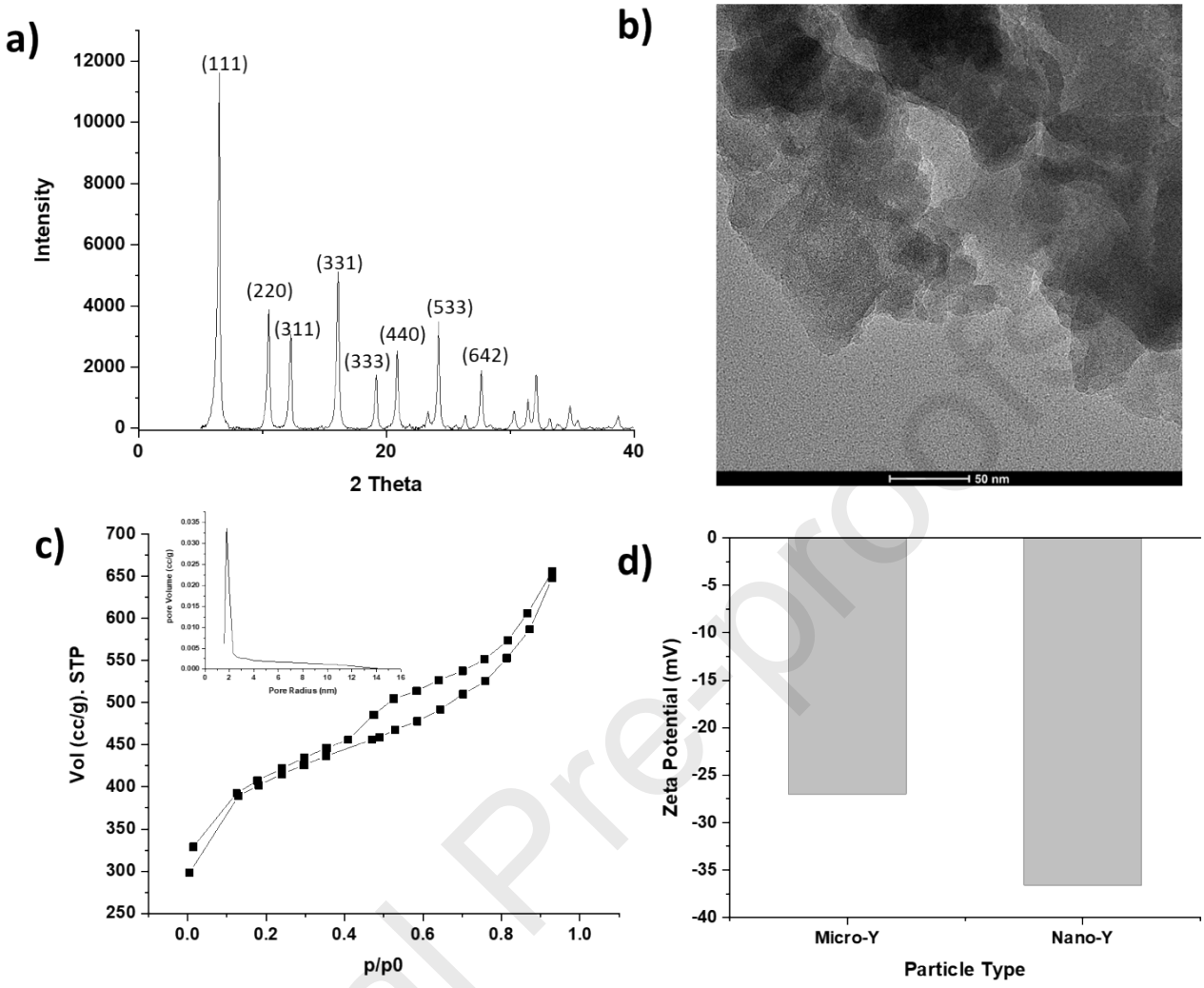

Figure 2: (a) XRD pattern, (b) TEM image , (c) N2 adsorption/desorption curves with inset of BJH pore size distribution for zeolite nano-Y, and (d) Zeta potentials for micro-Y and nano-Y particles.

3.2 Effect of Nano-Y on Membrane Structure

Figure 3a shows the XRD patterns for neat PSf and nano-Y/PSf membranes. An amorphous PSf structure was obtained as evident from the broad diffraction peak at 2θ value of approximately 17° (Figure 3b). M0.2 and M0.4 showed similar XRD patterns to the neat PSf membrane. No zeolite peaks were detected in low nano-Y concentrations, indicating good dispersion of the nano-Y within the PSf. Similar observation has been reported in [26, 34], where no XRD peaks

were obtained for phases with low concentrations. With an increase in nano-Y wt.%, above 0.6 wt. %, characteristic peaks of zeolite-Y were registered at 2θ values of 6.3° and 12.1°, highlighted by the arrow in Figure 3c. M1.5 showed slight peak broadening indicating that the incorporation of nano-Y (and more possibly its agglomeration) within the PSF matrix may have caused polymer chain disorder.

Surface chemistry of neat PSf and nano-Y/PSf membranes were determined by FTIR–ATR. FTIR allowed the identification of several functional groups present in the membrane. Spectra of PSf and nano-Y/PSf membranes in the range from 650 to 4000 cm^{-1} are shown in Figure 4a, while Figure 4b shows the same spectra in a range from 650 to 2000 cm^{-1} for a clear band identification. There is an obvious broad band at 3500 cm^{-1} (Figure 4a) corresponds to –OH. Characteristic bands of PSf were registered; 2970 cm^{-1} 1585 cm^{-1}, 1241 cm^{-1} and 1000-1250 cm^{-1} corresponds to -CH stretching, benzene stretching, C-O-C stretching and --S=O functional groups respectively. Figures 4(c-d) show FTIR spectra of nano –Y. The characteristic bands of Si-O and Al-O in the 1100–950 cm^{-1} range can be clearly observed in Figure 4d. These bands might be considered to be overlapped with the C-O stretch band in Figure 4b.

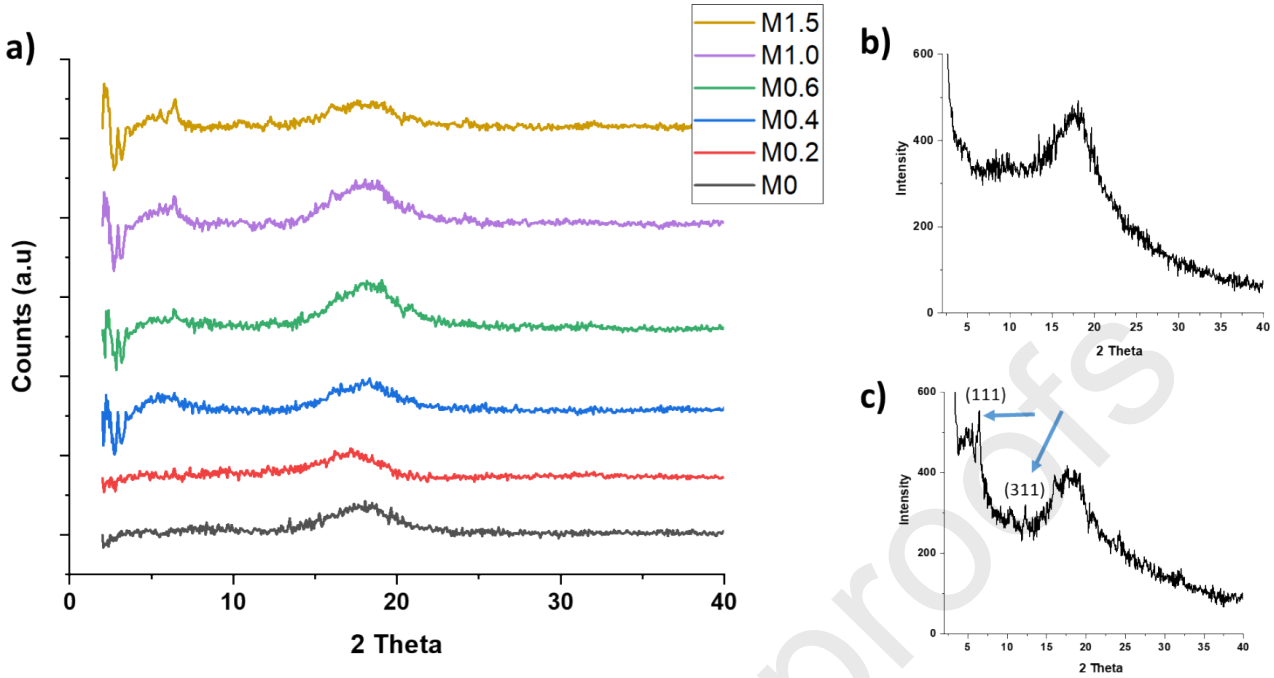

Figure 3: XRD patterns for (a) Membranes M0 to M1.5 (b) Membrane M0 and (c) Membrane M1.5

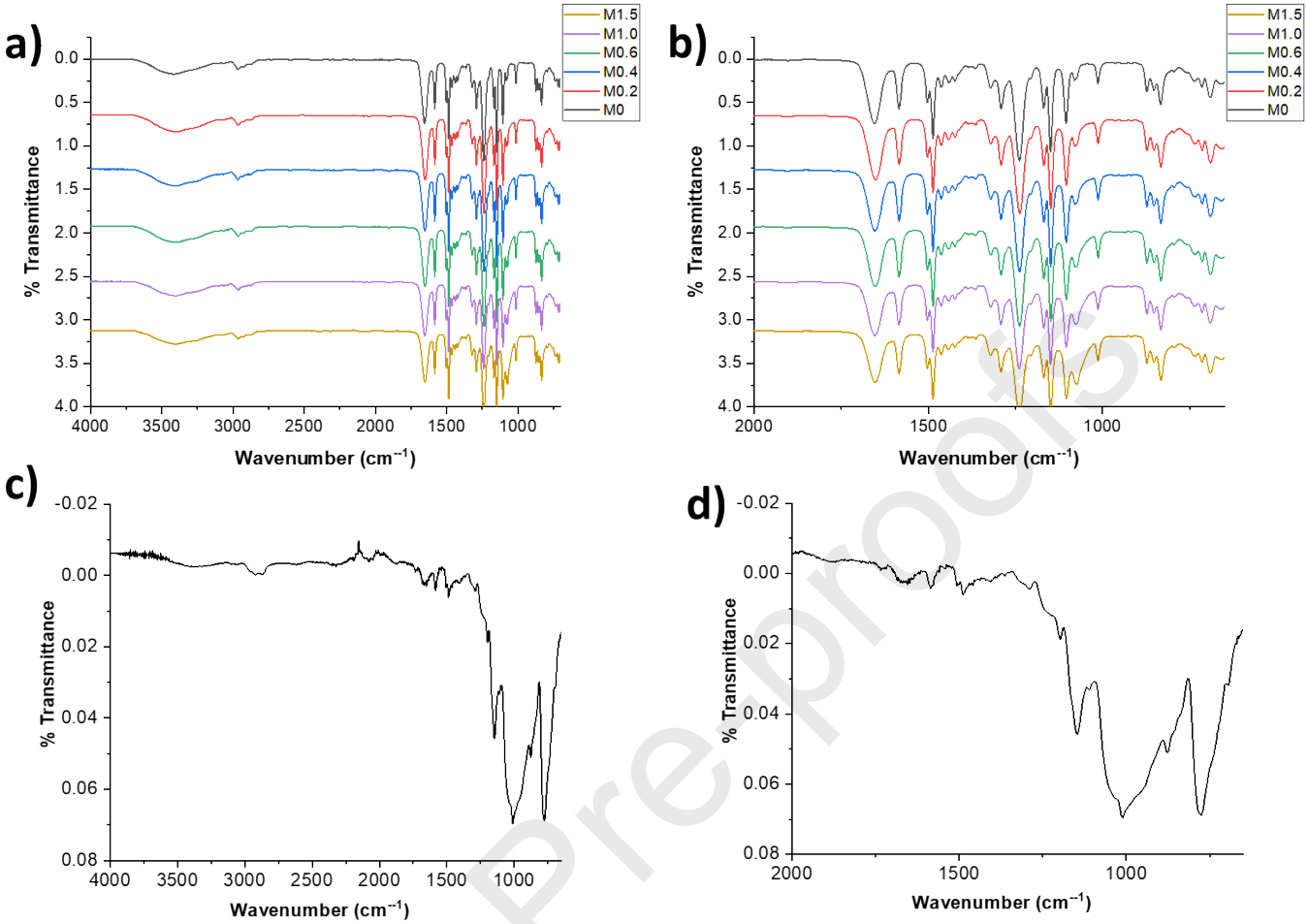

Figure 4: FTIR-ATR spectrums for neat (a-b) PSf and nano-Y/PSf membranes (c-d) nano Y

3.3 Membrane Morphology

Membrane morphology evolution for membrane surface and its cross section was studied through SEM at different magnifications. Figure 5 shows SEM images for the membranes M0 to M1.5. The first column shows membrane's top surface; the middle column depicts membrane's bottom surface and the third column is a magnified image of the corresponding bottom image in the second column. The top SEM images for all membranes show a dense, more nodule-like structure, typical of a phase inversion process for a viscous dope solution. Strong interactions between zeolite nanoparticles and PSf due to zeolite's high surface area and inter-hydrogen

bonding resulted in an increase in the casting solution viscosity giving dense top layers, and resulting in membranes with smaller pores. In addition, the phase inversion process usually slows down and the spinodal de-mixing may be the cause of the formation of a dense, selective top layer, similar to reported in [18]. Zeolite nanoparticles become more visible on the membrane's top surface with increasing nano-Y loading. For M1.0 and M1.5, zeolite nanoparticles were seen to be agglomerated more densely compared to the other membranes. This also hints towards poor contact between the polymer matrix and the nano-Y, where most of the nanoparticles is not embedded within the polymer, producing void defects and thus lowering the membrane's performance. The bottom surface of the membranes as shown in the SEM images of the second column reflect a porous structure. Again, this is typical of a phase inversion process, producing an asymmetric membrane structure, with a dense selective layer on top, and a porous sub layer on the bottom. The third column showing magnified bottom SEM images clearly shows the well-connected membrane pores. Again, nanoparticle agglomeration is visible for higher nano-Y concentrations beyond 0.4 wt.%, such as in M0.6 (Figure S1), where membrane pores can be clearly seen to be blocked by nano-Y. Pore blockage indicates the blockage of pores for water passage, hence reducing water flux (see section 3.7).

Figure 6 shows SEM images of cross-sections for the membranes M0 to M1.5. For M0 to M0.4, atypical cross-sectional microstructure was revealed by the images, where a sponge-like structure was formed, instead of finger-like pores. Again, a dense top layer is clearly visible for the membranes, as also highlighted by the arrow in Figure 6a. During the phase inversion process, this skin layer limits the penetration of the non-solvent (DI water in this case) into the proceeding sublayers and thus prevents further nuclei formation. For low PVP concentrations, the growth

rate is fast and macrovoid formation is inevitable. However, for a high concentration and molecular weight of PVP such as that used in this study, the growth rate slows down leading to a thick, dense top layer. Hence, the slow diffusion rate of the solvent plays a dominant role in this case, leading to a more sponge-like structure rather than finger-like pores. For most part of the membrane, a sponge-like structure was obtained indicating enough nuclei formation to suppress the macrovoids. Matsuyama et al. [35] have reported these structures for PSf and PVP concentrations of 15wt.% and 10 wt.% respectively. Kang and Lee [36] have reported similar findings where finger-like structures were suppressed by addition of a high molecular weight PVP porogen during polyacrylonitrile membrane formation. This phenomenon is only possible for dope solutions made from high polymer concentrations with high molecular weights, which would avoid the diffusion exchange rate of solvent and non-solvent in the membrane sub-layer, thus slowing the precipitation rate of the sub-layer, while encouraging fast phase separation in top layer.

Interestingly, membrane morphology was observed to change with progressive nano-Y additions for membranes M0.6 to M1.5 (Figures 6d-f). Membrane cross-section changed from a sponge-like structure to where macrovoid formation was evident. Usually, with nano zeolite additions, macrovoids in the sublayer have been reported to become more obvious [13] due to the hydrophilic nature of the nano-Y. During phase inversion, as soon as the membrane is immersed in the water bath, nano-Y would strongly adsorb water due to its strong interaction with it, leading to instantaneous liquid-liquid demixing. Thus, even with high polymer concentration solutions, a high content of nano-Y could produce macrovoids in the sublayer. Nevertheless, sponge-like structures have been reported to have a positive impact on separation mechanisms

involving large molecular weight contaminant molecules [37] compared to sublayers involving finger-like or macrovoids.

For low nano-Y concentrations, such as in M0.2 and M0.4, zeolite nanoparticles were seen to be uniformly distributed within the membrane's structure. Figure S2 confirms the presence of nano-Y through SEM-EDS for M0.2, where the different EDS spectra in Figure S2b corresponds to the EDS spots in Figure S2a. Figure 7a shows the cross sectional image of M0.4 at a higher magnification than Figure 6c, where nano-Y can be observed to be located at the mouth of the pores, however, no pore blockage can be observed. Figure 7b confirms the presence of the nano-Y particles through SEM-EDS analysis where the zeolite nanoparticles were detected at the pore entrances. The dashed boxes highlight the nano-Y situated at the abundant pore mouths. A weak Si and Al signal in this case can be due to the well dispersed nanoparticles present within the matrix, unlike in Figure S1 where strong signals were registered due to agglomeration. With high nano-Y loadings, nanoparticle agglomeration comes into effect which eventually again increases the top layer, slowing down the de-mixing effect. Figure S1b shows the cross-sectional SEM image of M1.5 where the dotted boxes indicate nano-Y agglomeration, and the corresponding EDS spectrum confirms the zeolite presence for the EDS spot indicated on the figure highlighted within the dotted box. Agglomeration is common issue with zeolite nanoparticles [24], owing to their high surface energy of the particles, they tend to cluster and hence this causes a limitation in their effective surface area.

Both, the top selective layer, and the porous sub layer hold significant roles in selectivity and water transport property. SEM analysis on nano-Y/PSf membranes revealed that zeolite nanoparticles were embedded both in the selective layer, as well as throughout with membrane

thickness, indicative of fast flow paths formed within the nano-Y nano channels and the whole membrane structure.

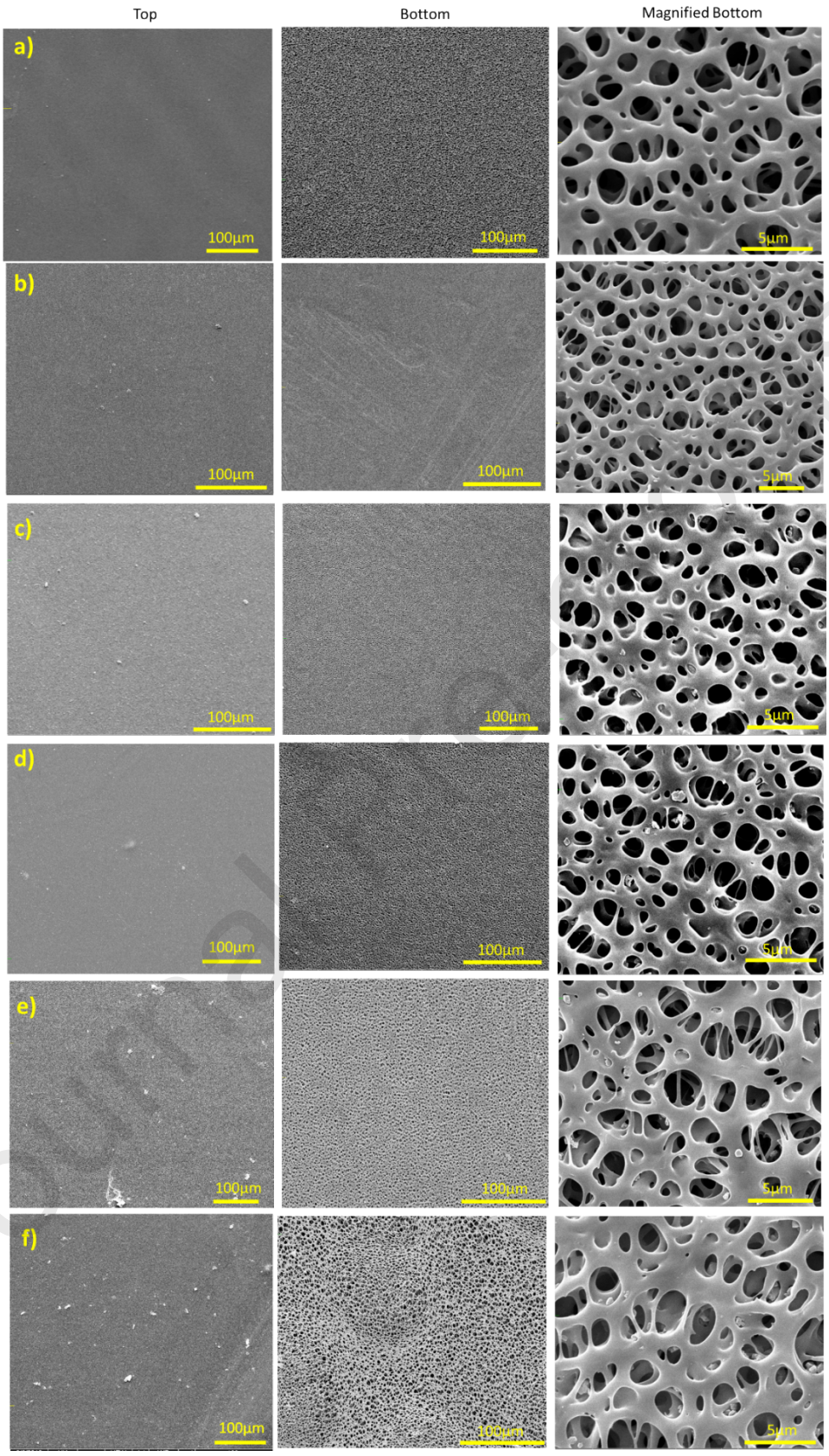

Figure 5: SEM images of top, bottom and magnified bottom for (a) M0, (b) M0.2, (c) M0.4, (d) M0.6, (e) M1.0, and (f) M1.5 membranes.

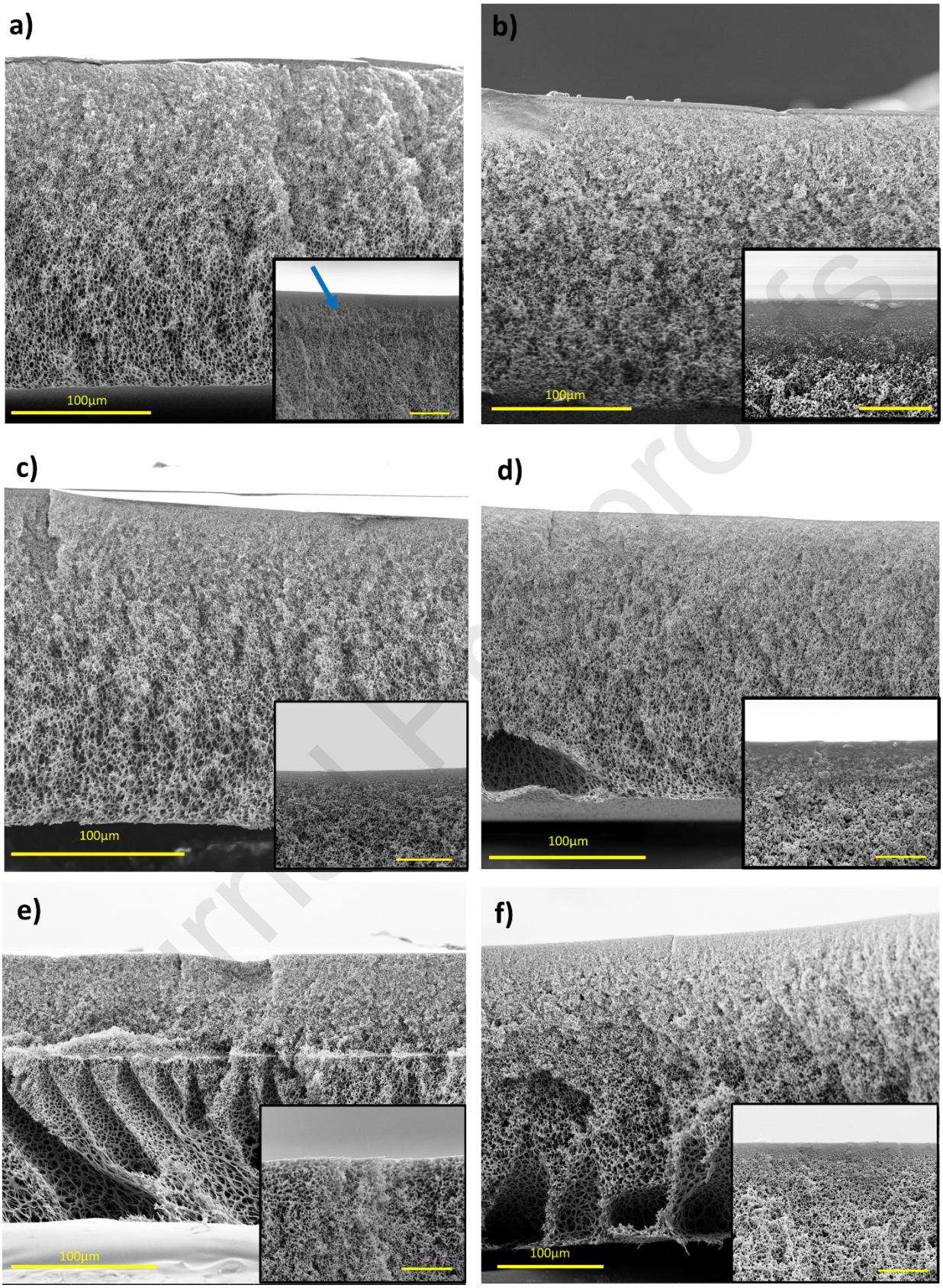

Figure 6: Cross-sectional images for membranes (a) M0, (b) M0.2, (c) M0.4, (d) M0.6, (e) M1.0, and (f) M1.5 (inset scale= 5µm).

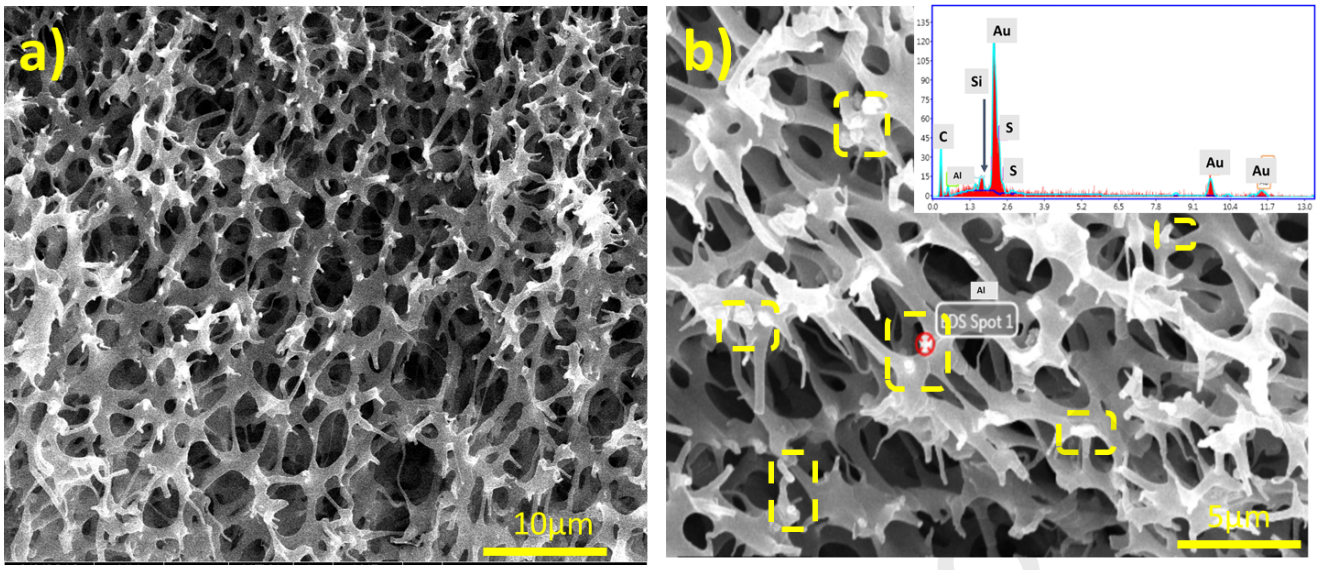

Figure 7: (a)Cross-sectional SEM image of M0.4 showing uniform nano-Y distribution, and (b) Cross-sectional SEM image of M0.4 at a higher magnification confirming the presence of nano-Y through EDS spectrum corresponding to the EDS spot 1 on the image. The dotted boxes highlight the presence of nano-y at the pore mouths.

3.4 Membrane Porosity and Pore Size

The variation in membrane porosity with progressive zeolite loading is shown in Figure 8. M0 gave a porosity of 86 %, which was seen to increase with nano-Y additions. Membranes M0.2 to M1.5 gave similar porosities of about 90% within the error range. Porosity increment with nano-Y addition may be attributed to the hydrophilic effect of nano-Y which expedited the solvent and non-solvent exchange during the phase inversion process. Wang et al. [38] has reported a similar observation with their PVDF membranes.

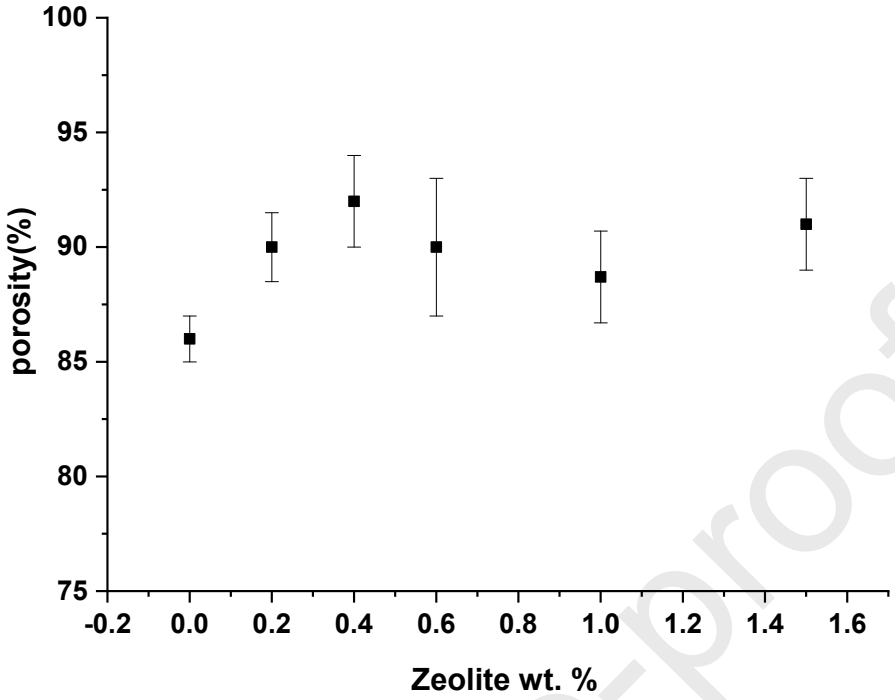

Figure 8: Variation in membrane porosity with nano-Y addition

BET method was used to characterize the surface area and pore size distribution in the membranes. Figure S3 shows N_2 adsorption/desorption isotherms of the membranes from M0 to M1.5 in the relative pressure (P/P_o) range of 0.05 to 0.99. The BET surface area for M0, M0.2, M0.4, M0.6, M1.0 and M1.5 was found to be 19, 23, 28, 34, 30 and 34 m^2/g respectively. A gradual increase in BET surface area was observed with nano-Y addition. Zeolite loadings used in this study are quite low and hence an enormous effect in surface area variation is not evident with such low loadings where the host polymer is in high concentration, hence defining the major part of the surface area.

Pore size distribution of the membranes was calculated using the BJH-model. The average pore size of neat PSf was found to be around 8 nm, with pore radius range from 2 to 50 nm. Such small

pore sizes are consistent with literature where 15 wt.% PSf and 10 wt.% PVP concentrations were used to fabricate UF membranes [39]. With such a dope composition, the membrane's surface becomes denser and less porous, as also attributed from the SEM images (section 3.3). Pore radii in all other membranes with nano-Y additions were found to be in similar range as PSf, with pore radii peaking at 2 nm and 15 nm.. Addition of nano-Y did not significantly alter the mean pore diameter of the membrane. Uniform nanoscale dispersion of zeolite nanoparticles in dope solution lead to small size nodules, resulting in small average pore sizes. However, the pore size distribution was seen to slightly change for high nano-Y loadings. M1.5 showed an enhanced %distribution, where most of the pores were in two ranges; 1.5-2 nm and 10-15 nm. The pore size range clearly shows a mesoporous membrane character, as also evident by the shape of the BET curves.

3.5 Membrane Wettability

Addition of zeolite nano-Y brought about a change in the membrane's surface properties in terms of its hydrophilic behavior. Figure 9 shows the variation in water contact angle of PSf and nano-Y/PSf membranes. Neat PSf membrane showed a contact angle of 73.4^{o}. Similar contact angles for PSf membranes have been reported in the literature [4, 14]. A decrease in contact angle from 73.4^{o} to 64.2^{o} and 54.5^{o} was registered with progressive zeolite nano-Y addition of from 0.2 wt. % to 0.4 wt. %. The embedment of nano-Y into PSf bulk due to hydrogen bonding interaction between the sulfonic group of PSf and –OH group in zeolite [18] gave better hydrophilicity for M0.2 and M0.4 membranes. This improved hydrophilicity is suggestive to improve water flow through the membranes and hence reduce water flow hindrance along the membrane. A vast 10^{o} difference in contact angle between M0 and a slight nano-Y addition of 0.2 wt.%, and then

0.4 wt.% nano-Y is apparently due to the well-dispersed zeolite within the polymeric matrix as also highlighted in section 3.3. In addition, the high SiO_2/Al_2O_3 ratio of 30 used in this study usually produced an pronounced effect on membrane hydrophilicity as also reported [26, 40]. Almost a constant contact angle was observed after 0.4 wt.% nano-Y addition. Thus, a further increase in nano-Y did not bring about a significant decrease in contact angle.

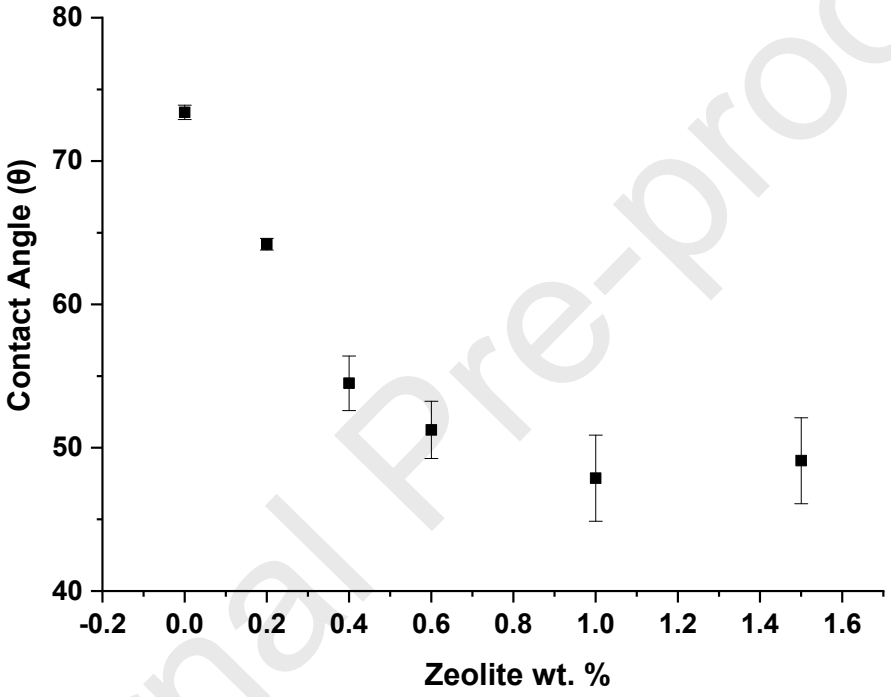

Figure 9: Water droplet contact angles for neat PSf and nano-Y/PSf membranes.

3.6 Thermal Stability

Thermal behavior of the membranes, M0 to M1.5 were studied through DSC and TGA methods. DSC was used to help us identify any difference in T_g on addition of nano-Y loadings. T_g is indicative of the measure of the degree of rigidity of the polymer chains. As T_g is not a fixed value,

but rather a range, Table 2 shows the range of Tg values (its onset, middle and end) for the membranes synthesized, while Figure 10 shows the DSC curves from 100˚C to 250˚C temperature range, from which these T_g values were obtained. The black dots on the DSC curves correspond to the middle T_g values for each respective membrane. The bare PSf membrane showed a T_g of 185.8 ˚C. Similar values have been reported in the literature for PSf membranes [18]. The range in T_g for each membrane (T_g end-T_g onset) narrowed down from M0 (6.7˚C) to M0.4 (5.5 ˚C), after which it again increased, with M1.5 showing a wide range in T_g of about 10˚C. A clear decreasing trend in T_g can be observed on progressive nano-Y loadings, indicating lower thermal resistance. Hence, this indicates that the polymer transition from glassy to rubbery zone is occurring at a lower temperature. Hence, with the addition of nano-Y, a more flexible conformation rearrangement of PSf macromolecules chains occurred. Nevertheless, the decrease in the Mid T_g from M0 to M0.4 membranes is not drastic, but only of a few degrees≈ 5 ˚C. However, higher nano-y loadings such as those in M1.5 showed a much lower T_g compared to PSf, decreasing from 185.8 ˚C to 174.7 ˚C. Above room temperature process during dyeing in textile industries usually generates high temperature wastewaters [41]. Thus, membranes with lower T_g, such as those with high zeolite loadings become less resistance to such processes for treating dye wastewaters. Lower T_g <140 ˚C with other zeolite types have been reported in the literature.

Figure S4 shows the TGA curves for the membranes from M0 to M1.5. Neat PSf membranes start to lose weight at around 450 ˚C, which remained almost the same for all the other membranes, thus indicative of PSf's thermal decomposition. Zeolites on the other hand is thermally stable up to high temperatures above 1000 ˚C. Hence, from the DSC and TGA studies, it was concluded that nano-Y addition did not significantly alter the thermal properties of PSf membranes, especially at

lower zeolite loadings. While the thermal decomposition behavior of nano-Y/PSf membranes showed no obvious change compared to bare PSf, the Tg for higher zeolite loadings gave much lower values, deeming the material unsuitable for UF dye application with high wastewater temperatures.

Table 2: Onset, Mid and End Tg for M0 to M1.5 membranes

Membrane	T_g Onset (˚C)	T_g Mid (˚C)	T_g End (˚C)
M0	182.4	185.8	189.1
M0.2	177.8	180.8	184.6
M0.4	178.0	180.6	183.5
M0.6	177.5	183.4	183.6
M1.0	176.3	179.2	183.1
M1.5	170.8	174.7	180.3

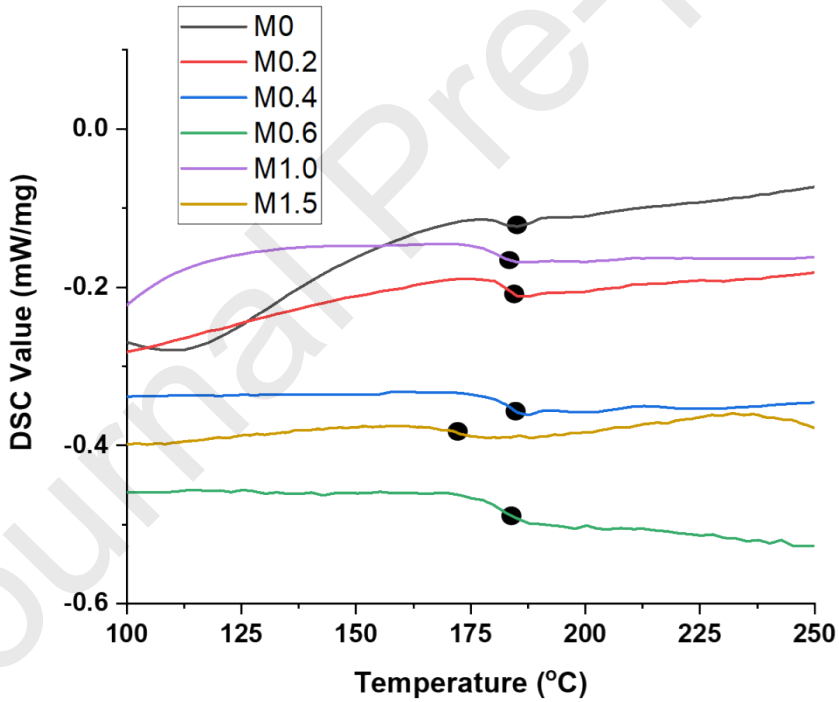

Figure 10: DSC graphs from M0 to M1.5 membranes, with the black dots highlighting the Mid Tg for each membrane.

3.7 Ultrafiltration Performance

Pure water flux for the membranes M0 to M1.5 for testing pressures 2, 4 and 6 bars is shown in Figure S5. All membranes showed an almost linear increase in flux with applied pressure, consistent to several previous studies [37, 42]. For a fixed feed concentration, the effective driving force for solvent transport increases with increase in pressure. The driving force overcomes the membrane resistance hence forcing more water to pass through the membrane with for higher pressures. The pure water flux for M0 increased from 100±5 $L.m^{-2}.h^{-1}$ at 2 bars to 254±3.5 $L.m^{-2}.h^{-1}$ at 6 bars. On addition of nano-Y, water permeation of the membrane was improved, as shown by increased PWF for the nano-Y/PSf membranes. With increasing nano-Y content, the PWF flux increased to 525±5 $L.m^{-2}.h^{-1}$ for M0.4. This was almost double than the initial water flux obtained for neat PSf membrane. This pattern of increasing flux for nano-Y has also been reported in [26] for RO application. The maximum water flux was obtained for M0.4 which might be due to the uniform nano-Y distribution throughout the membrane thickness. The micro- and nano-channels in zeolite facilitates easier flow of water molecules when present at the mouth of the pores. Beyond 0.4 wt. % nano-Y, flux was observed to gradually decline reaching a minimum of 150 $L.m^{-2}.h^{-1}$ at 6 bar for M1.5. The decrease in flux might be attributed to pore blockage due to nanoparticle agglomeration (Figure S1). As the membrane surface is the first place to come into contact with the non-solvent phase, the migration of zeolite nanoparticles to the top is apparent, and leads to accumulation of nano-Y on membrane's surface posing hindrance to the water passage. Similar decrease in PWF with high nano zeolite loadings have been reported for UF membranes by Moradihamedani and Abdullah [19] and Han et al. [13].

To study the effect of nano-Y addition on CVD dye rejection and corresponding permeate flux, all membranes were tested for MEUF experiments at a similar pressure of 6 bar. Surfactant-dye interactions have been reported in the literature [43, 44] where spectral studies have concluded the importance of both electrostatic and hydrophobic forces between ionic dyes and ionic surfactants. In this study, the negatively charged SDS and the positively charged CVD dye interact with each other to form micelles, hence facilitating dye rejection for the small size CVD molecules. Figure 11a shows the variation in permeate flux with increasing nano-Y percentage. Much lower permeate flux values were obtained compared to the PWF. This is because the micelles formed during the dye-surfactant interaction are big in size and hence get accumulated on the membrane's surface consequently resulting in a higher surfactant concentration over there. Studies by Sharma and Purkait have reported analogous observations regarding concentration polarization [29]. An initial permeate flux of 60 $L.m^{-2}.h^{-1}$ was obtained for M0, which showed a gradual increase to 90 $L.m^{-2}.h^{-1}$ and 105 $L.m^{-2}.h^{-1}$ for M0.2 and M0.4 respectively. Nano-Y is a FAU zeolite having a 3-D channel structure which provides a high water permeability compared to other 1-D zeolite structures such as LTL [26]. Its internal porosity forms preferential water pathways, hence enhancing the water permeability through the zeolite. However, the flux abruptly dropped to 40 $L.m^{-2}.h^{-1}$ for M0.6 and M1.0 membranes, reaching a minimum of 30 $L.m^{-2}.h^{-1}$ for M1.5. Membrane hydrophilicity and morphology are important factors governing membrane permeability and selectivity. The trend in flux decrease is similar to what was observed for PWF owing to pore blockage by the nanoparticle aggregates. Apart from agglomeration within the membrane structure, the aggregates formed on the membrane's surface also contribute to flux decline by forming an additional resistance layer. Thus, even with an increased membrane hydrophilicity, the effect of facial pore blockage comes into play leading

to reduced membrane performances. Nevertheless, the obtained flux values in this study for dye rejection is greater than those reported in the literature (Table 3). Interestingly, the initial permeate flux for the bare PSf membrane for CVD rejection was also higher than those reported previously, mostly owing to the high porosity and membrane morphology obtained for the present membranes. Nevertheless, similar permeate fluxes have been reported for another zeolite/PSf membranes for other contaminant rejections such as Bovine serum albumin [18].

Figure 11b shows CVD rejection for MEUF experiments. M0 gave a rejection of around 60%, which increased with progressive nano-Y addition to 88% and 99.5% for M0.2 and M0.4 respectively. The rejection obtained by M0 in this study is quite high for an UF membrane, and thus can be attributed to the membrane's tighter structure and the fact that the dye molecules were solubilized on the surfactant micelles and hence retained by the UF membrane. Only a small wt. % of nano-Y was sufficient to enhance the UF performance, unlike several of the previous studies which report high zeolite loadings for optimum performances [13, 19]. Figure 12 shows a schematic of the various possible dye-membrane interactions which can occur. Globular micellar sizes for SDS have been reported to be around 2.5nm with an aggregation number of 70 [45] which defines the number of molecules present in a micelle once CMC has been reached. Thus, the UF membranes rejects the surfactant micelles through the size exclusion principle, and hence does not let the bigger, aggregated molecules pass through the membrane pore. In addition, the nano-Y situated on the pore entrances blocks the micelles from entering the membrane pores as the zeolite micro- and mesopores are smaller than the dye molecules. A uniform distribution of nano-Y in M0.4 accounted for a high dye rejection of 99.5%; apart from size exclusion, electrostatic interactions where due to similar charges, the anionic surfactant molecule repels

the negatively charged zeolite particles present at the pore openings increases the rejection. For the insolubilized cationic dye molecules, these can either pass through the membrane, or get adsorbed on the zeolite particles. Thus dye adsorption helps in further rejection. Moreover, the high surface area of the nano-Y provides better accessibility to the active sites and hence ion exchange increases further helping with a higher rejection. With a further increase in nano-Y content beyond 0.4 wt. %, the rejection was seen to progressively decrease to 81%, 40% and 23% for M0.6, M1.0 and M1.5 membranes respectively. Such a trend of decrease in rejection with increasing doping content is also reported in previous studies for various different nanofillers embedded in PSf membranes [18, 46]. This decrease again might be associated with nanoparticle agglomeration. Agglomeration also causes defects in the membrane, especially on its surface where the interaction of nano-Y and the polymer is the lowest, hence leading to low separation efficiencies. Secondly, the decrease in rejection an also be due to a change in membrane morphology for M0.6 to M1.5 (section 3.3) with increasing nano-Y, we observed formation of more macrovoids, and hence it is well reported in the literature that for most large molecular weight contaminant molecules, sponge like structures are more favorable for high contaminant rejections [37].

Dye rejection experiments were also carried out without SDS. Figure S6 shows the flux and dye rejection for CVD when no surfactant was used. Low rejections were obtained as expected. Interestingly, an increasing rejection trend was obtained contrary to when the feed was mixed with SDS. This increase in CVD rejection with increasing nano-Y addition might be attributed to dye adsorption, which increases with the loading. The adsorption for organic contaminants is more pronounced in FAU type zeolites with higher Si/Al ratio [47]. The cationic dye readily

adsorbs onto zeolite, however, with the lack of enough adsorbing sites and its low molecular size, the rejection of CVD is quite low. Hence, it is clear that the dye molecules become solubilized on surfactant addition, and the micelles formed are much bigger in size to enhance dye retention. Another interesting result was the permeate flux obtained for CVD rejection (Figure S6a). Higher flux was obtained compared to when SDS was used. This may again be due to the formation of micelles which are bigger in size than the membrane pores and hence get accumulated on the membrane surface, consequently leading to increased surfactant concentration near the surface than the bulk, and participating in flux reduction. In addition, the flux for CVD showed a similar pattern to CVD/SDS, where the highest flux was recorded for M0.4 for the reasons already discussed in this section. Over the period of time, overlapping double layers may develop due to ion adsorption. Since, the rejection increases with zeolite addition, we can conclude increasing ion adsorption, and hence increase in the charged layers which can slow down water transport due to the polarized water molecules interaction with the immobile charged surface.

Figure 11c shows the variation in permeate flux and dye rejection for M0.4 over time. An initial increase in dye rejection was observed with time from 99.2 to about 99.5%. This small increase might be due to dye solubilization within the surfactant micelles, which were in turn retained over the membrane's surface due to its larger size. Rejection and flux were both stabilized after a certain time, with the flux initially dropping from 107.5 to about 105.0 $L.m^{-2}.h^{-1}$ after 80 min and remaining constant thereafter. During dye filtration, reduction in membrane flux is unavoidable due to the effect of fouling. Fouling may be caused by the adsorption of dye molecules [48] on the membrane surface and its pores. FRR is a measure of the antifouling property of the membrane, which indicates the ability of a membrane to recover its initial water

flux after cleaning with DI water. Figure 13 shows the FRR for the membranes M0 to M1.5. M0 and M0.2 registered similar FRRs, while a slightly higher FRR of 90% was obtained for M0.4. The FRR dropped drastically to 66% for higher nano-Y concentration of 1.5 wt. %. The uniform distribution of the nano-Y on the membrane's skin layer results in improved hydrophilicity, and hence increased antifouling ability for M0.4. Hydrophilic surfaces do not adsorb dye molecules easily and thus restricts membrane fouling. In addition, MEUF Zeolite nano-Y possess special functional properties including its nano-size, abundant flow channels, high surface area, a negative charge and it small pore sizes allowing water molecules to pass through it while restricting the passage of micelles rendering high solute rejections through steric exclusion and donnan principle. Figure S7 shows the M1.0 membrane after filtration. Both membrane top and bottom SEM images show no obvious change in membrane morphology. The EDS spots in Figure S7b and their corresponding spectra in Figures S7(c-d) confirm the presence of nano-Y after membrane use.

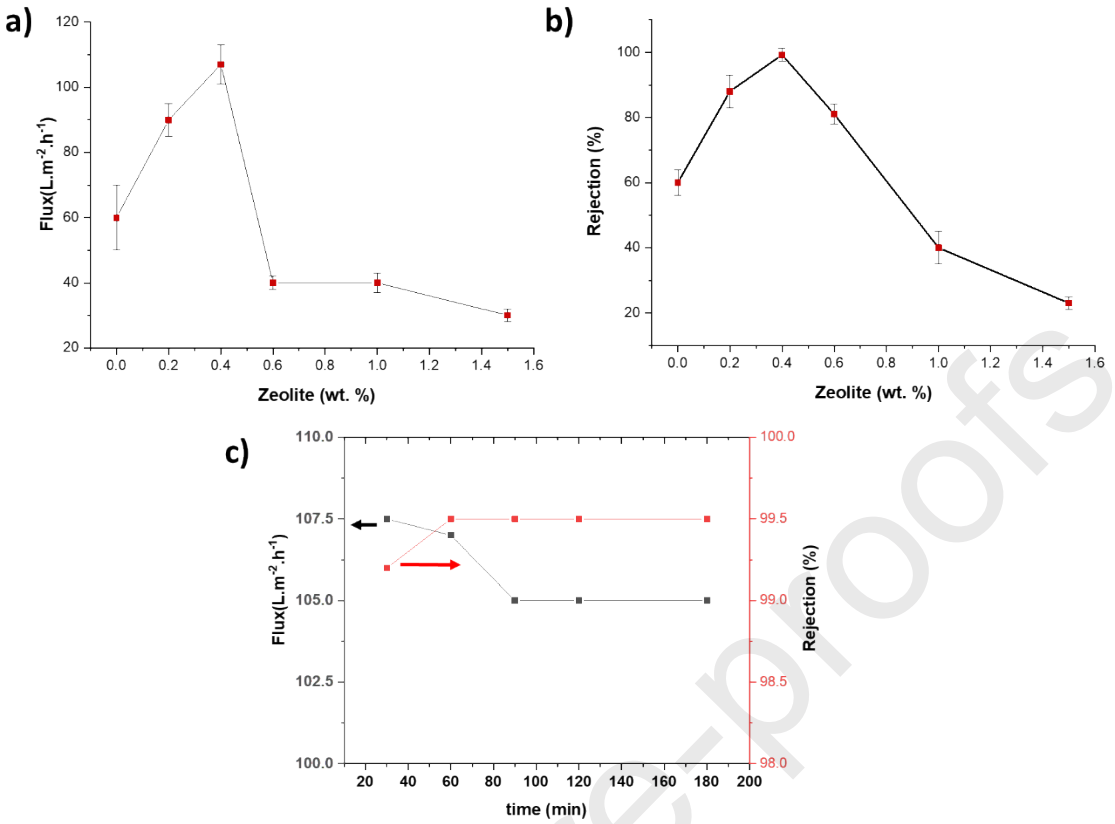

Figure 11: (a) Flux and (b) Dye Rejection with increasing nano-Y loadings (c) Variation in flux and dye rejection over time for M0.4 membrane

Table 3: Literatures related to CVD removal.

Membrane Type/ Reference	Flux (L/m^2.h)	Pressure (kPa)	Rejection (%)	Reference
Nanofiltration membrane	7.55	415	95	[49]
Microfiltration prior to advanced oxidation process	13.2	276	100	[50]
Nanofiltration membrane	11	700	98	[51]
Hollow fiber nanofiltration membrane	5.57	70	99.2	[52]
PSf with Dextro-tartaric acid and DL-tartaric acid additives (MEUF)	13.2	150	99	[29]
Nano-Y/PSf UF membrane (MEUF)	107	600	99.5	This study

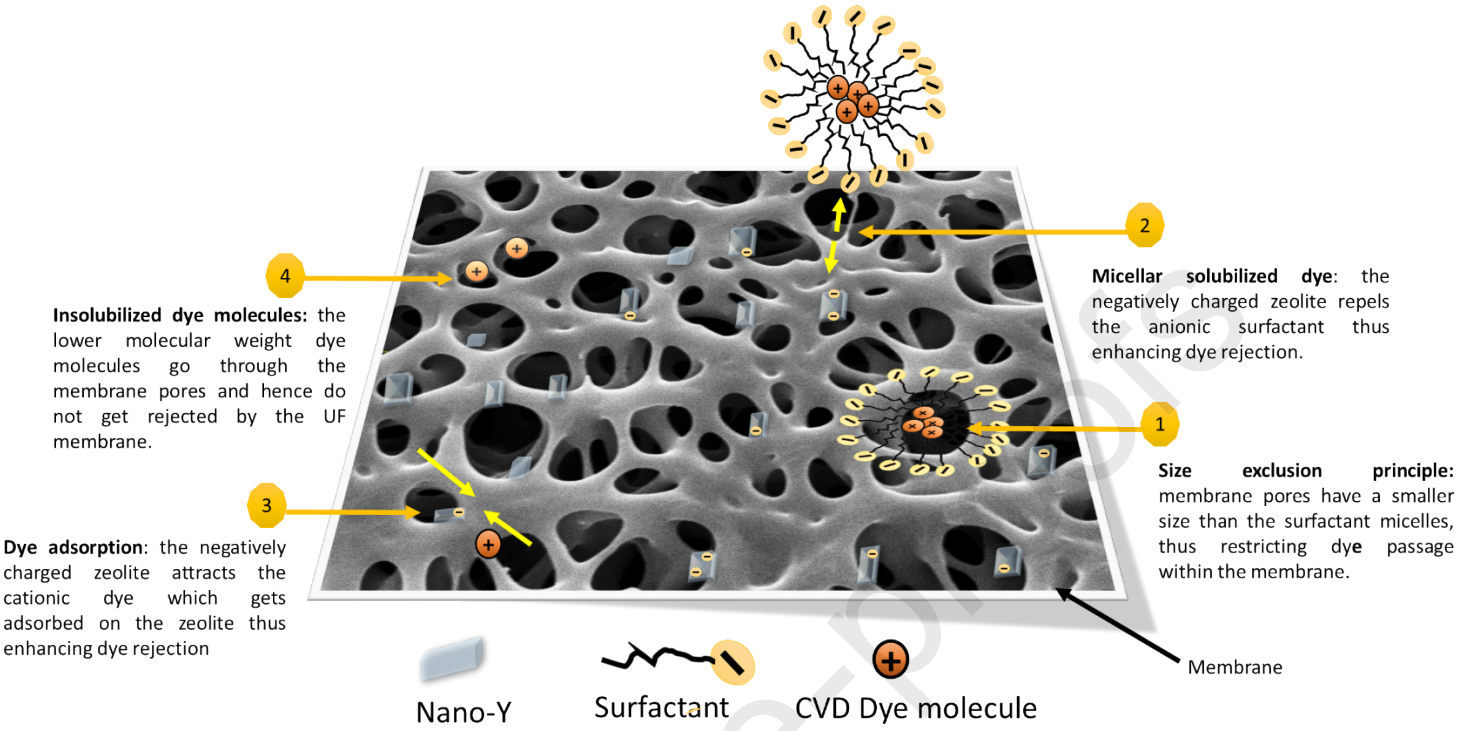

Figure 12: Schematic representing possible membrane-dye interactions

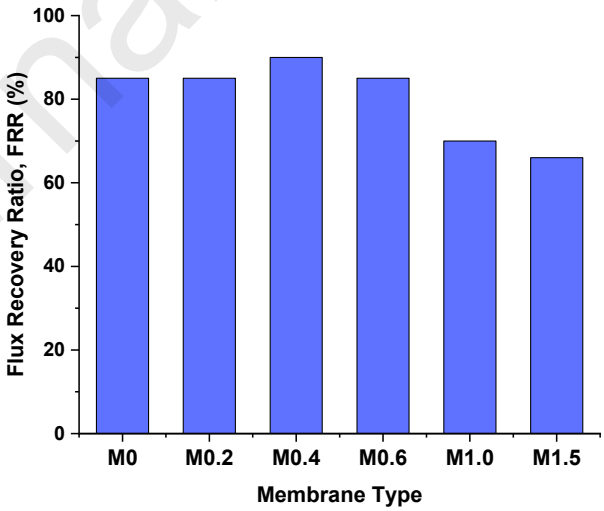

Figure 13: Flux recovery ratio of PSf and nano-Y/PSf membranes.

4. Conclusion

MEUF is an important technique that can facilitate the removal of many of the industrial pollutants such as heavy ions, organics and dyes. In the present study, UF membranes made from PSf and nano-Y zeolite were fabricated through the phase inversion method. Nano-Y with a high SiO_2 to Al_2O_3 ratio of 30 was produced through ball milling of micron-sized zeolite-Y particles. Membrane morphology through SEM revealed a sponge-like pore structure, with the nano-Y uniformly distributed throughout the membrane structure and the opening of the pores for low zeolite concentrations. Membrane hydrophilicity was enhanced with nano-Y addition, with 0.4 wt. % nano-Y loading giving a contact angle of 54.5^o. Dye rejection experiments were conducted for MEUF, whereby dye molecules were successfully rejected by nano-Y/PSf membranes giving a higher flux and rejection of about 105 $L.m^{-2}.h^{-1}$ and 99.5% respectively compared to neat PSf membrane with 60 $L.m^{-2}.h^{-1}$ flux and 60.0% rejection. Thus, addition of nano-Y in PSf matrix had a strong impact on the phase de-mixing of the casting suspension, forming a thin dense layer on the top for small loadings, and a uniform nano-Y distribution at the pore openings which restricted the passage of dye through electrostatic interactions. The membranes also showed good resistance to fouling as evaluated from their high flux recovery ratios reaching almost 90%.

5. Acknowledgement

The authors would like to acknowledge the support and facilities of the Core Technology Platform at New York University Abu Dhabi.

6. References

[1] S.F. Anis, R. Hashaikeh, N. Hilal, Microfiltration membrane processes: A review of research trends over the past decade, Journal of Water Process Engineering, 32 (2019) 100941.
[2] M. Schwarze, Micellar-enhanced ultrafiltration (MEUF) – state of the art, Environmental Science: Water Research & Technology, 3 (2017) 598-624.
[3] A.L. Ahmad, S.W. Puasa, M.M.D. Zulkali, Micellar-enhanced ultrafiltration for removal of reactive dyes from an aqueous solution, Desalination, 191 (2006) 153-161.
[4] L.-x. Dong, H.-w. Yang, S.-t. Liu, X.-m. Wang, Y.F. Xie, Fabrication and anti-biofouling properties of alumina and zeolite nanoparticle embedded ultrafiltration membranes, Desalination, 365 (2015) 70-78.
[5] M. Ulbricht, Advanced functional polymer membranes, Polymer, 47 (2006) 2217-2262.
[6] J.R. Du, S. Peldszus, P.M. Huck, X. Feng, Modification of poly(vinylidene fluoride) ultrafiltration membranes with poly(vinyl alcohol) for fouling control in drinking water treatment, Water Research, 43 (2009) 4559-4568.
[7] S.F. Anis, R. Hashaikeh, N. Hilal, Functional materials in desalination: A review, Desalination, 468 (2019) 114077.
[8] Y.T. Chung, E. Mahmoudi, A.W. Mohammad, A. Benamor, D. Johnson, N. Hilal, Development of polysulfone-nanohybrid membranes using ZnO-GO composite for enhanced antifouling and antibacterial control, Desalination, 402 (2017) 123-132.
[9] X.-M. Wang, X.-Y. Li, K. Shih, In situ embedment and growth of anhydrous and hydrated aluminum oxide particles on polyvinylidene fluoride (PVDF) membranes, Journal of Membrane Science, 368 (2011) 134-143.
[10] S. Liang, G. Qi, K. Xiao, J. Sun, E.P. Giannelis, X. Huang, M. Elimelech, Organic fouling behavior of superhydrophilic polyvinylidene fluoride (PVDF) ultrafiltration membranes functionalized with surface-tailored nanoparticles: Implications for organic fouling in membrane bioreactors, Journal of Membrane Science, 463 (2014) 94-101.
[11] C.P. Leo, W.P. Cathie Lee, A.L. Ahmad, A.W. Mohammad, Polysulfone membranes blended with ZnO nanoparticles for reducing fouling by oleic acid, Separation and Purification Technology, 89 (2012) 51-56.
[12] A. Bouazizi, M. Breida, B. Achiou, M. Ouammou, J.I. Calvo, A. Aaddane, S.A. Younssi, Removal of dyes by a new nano–TiO2 ultrafiltration membrane deposited on low-cost support prepared from natural Moroccan bentonite, Applied Clay Science, 149 (2017) 127-135.
[13] R. Han, S. Zhang, C. Liu, Y. Wang, X. Jian, Effect of NaA zeolite particle addition on poly(phthalazinone ether sulfone ketone) composite ultrafiltration (UF) membrane performance, Journal of Membrane Science, 345 (2009) 5-12.
[14] Y. Yurekli, Removal of heavy metals in wastewater by using zeolite nano-particles impregnated polysulfone membranes, Journal of Hazardous Materials, 309 (2016) 53-64.
[15] M.S. Gaur, P.K. Singh, Suruchi, R.S. Chauhan, Structural and thermal properties of polysulfone-ZnO nanocomposites, Journal of Thermal Analysis and Calorimetry, 111 (2013) 743-751.
[16] S.F. Anis, G. Singaravel, R. Hashaikeh, Electropsun Ni-W/zeolite composite fibers for n-heptane hydrocracking and hydroisomerization, Materials Chemistry and Physics, 200 (2017) 146-154.
[17] G. Bonilla, M. Tsapatsis, D.G. Vlachos, G. Xomeritakis, Fluorescence confocal optical microscopy imaging of the grain boundary structure of zeolite MFI membranes made by secondary (seeded) growth, Journal of Membrane Science, 182 (2001) 103-109.
[18] F. Liu, B.-R. Ma, D. Zhou, Y.-h. Xiang, L.-x. Xue, Breaking through tradeoff of Polysulfone ultrafiltration membranes by zeolite 4A, Microporous and Mesoporous Materials, 186 (2014) 113-120.
[19] P. Moradihamedani, A.H. Abdullah, Preparation and characterization of polysulfone/zeolite mixed matrix membranes for removal of low-concentration ammonia from aquaculture wastewater, Water Science and Technology, 77 (2017) 346-354.
[20] M.A. Anderson, Removal of MTBE and other organic contaminants from water by sorption to high silica zeolites, Environmental science & technology, 34 (2000) 725-727.
[21] D. Klint, H. Eriksson, Conditions for the Adsorption of Proteins on Ultrastable Zeolite Y and Its Use in Protein Purification, Protein Expression and Purification, 10 (1997) 247-255.
[22] C. Zhou, J. Zhou, A. Huang, Seeding-free synthesis of zeolite FAU membrane for seawater desalination by pervaporation, Microporous and Mesoporous Materials, 234 (2016) 377-383.
[23] B. Zhuman, Saepurahman, S.F. Anis, R. Hashaikeh, Obtaining high crystalline ball milled H-Y zeolite particles with carbon nanostructures as a damping material, Microporous and Mesoporous Materials, 273 (2019) 19-25.

[24] S.F. Anis, G. Singaravel, R. Hashaikeh, Hierarchical nano zeolite-Y hydrocracking composite fibers with highly efficient hydrocracking capability, RSC Advances, 8 (2018) 16703-16715.
[25] S.F. Anis, R. Hashaikeh, Electrochemical water splitting using nano-zeolite Y supported tungsten oxide electrocatalysts, Journal of Nanoparticle Research, 20 (2018) 47.
[26] S.F. Anis, R. Hashaikeh, N. Hilal, Flux and salt rejection enhancement of polyvinyl(alcohol) reverse osmosis membranes using nano-zeolite, Desalination, 470 (2019) 114104.
[27] M. Mulder, Basic Principles of Membrane Technology, Kluwer Academic Publishers, Norwell, MA, U.S.A., 1996.
[28] K. Zodrow, L. Brunet, S. Mahendra, D. Li, A. Zhang, Q. Li, P.J.J. Alvarez, Polysulfone ultrafiltration membranes impregnated with silver nanoparticles show improved biofouling resistance and virus removal, Water Research, 43 (2009) 715-723.
[29] N. Sharma, M. Purkait, Enantiomeric and racemic effect of tartaric acid on polysulfone membrane during crystal violet dye removal by MEUF process, Journal of Water Process Engineering, 10 (2016) 104-112.
[30] B.S. Lalia, E. Guillen-Burrieza, H.A. Arafat, R. Hashaikeh, Fabrication and characterization of polyvinylidenefluoride-co-hexafluoropropylene (PVDF-HFP) electrospun membranes for direct contact membrane distillation, Journal of Membrane Science, 428 (2013) 104-115.
[31] S.K. Hait, P.R. Majhi, A. Blume, S.P. Moulik, A Critical Assessment of Micellization of Sodium Dodecyl Benzene Sulfonate (SDBS) and Its Interaction with Poly(vinyl pyrrolidone) and Hydrophobically Modified Polymers, JR 400 and LM 200, The Journal of Physical Chemistry B, 107 (2003) 3650-3658.
[32] A. Al-Ani, R.J. Darton, S. Sneddon, V. Zholobenko, Nanostructured Zeolites: The Introduction of Intracrystalline Mesoporosity in Basic Faujasite-type Catalysts, ACS Applied Nano Materials, 1 (2018) 310-318.
[33] A. Sachse, A. Grau-Atienza, E.O. Jardim, N. Linares, M. Thommes, J. García-Martínez, Development of Intracrystalline Mesoporosity in Zeolites through Surfactant-Templating, Crystal Growth & Design, 17 (2017) 4289-4305.
[34] S.F. Anis, G. Singaravel, R. Hashaikeh, NiW/nano zeolite Y catalysts for n-heptane hydrocracking, Materials Chemistry and Physics, 212 (2018) 87-94.
[35] H. Matsuyama, T. Maki, M. Teramoto, K. Kobayashi, Effect of PVP Additive on Porous Polysulfone Membrane Formation by Immersion Precipitation Method, Separation Science and Technology, 38 (2003) 3449-3458.
[36] J.S. Kang, Y.M. Lee, Effects of molecular weight of polyvinylpyrrolidone on precipitation kinetics during the formation of asymmetric polyacrylonitrile membrane, Journal of applied polymer science, 85 (2002) 57-68.
[37] N.a. Alia, H. Sofiah, A. Asmadi, A. Endut, Preparation and characterization of a polysulfone ultrafiltration membrane for bovine serum albumin separation: Effect of polymer concentration, Desalination and Water Treatment, 32 (2011) 248-255.
[38] Z. Wang, H. Yu, J. Xia, F. Zhang, F. Li, Y. Xia, Y. Li, Novel GO-blended PVDF ultrafiltration membranes, Desalination, 299 (2012) 50-54.
[39] C. Ding, J. Yin, B. Deng, Effects of polysulfone (PSf) support layer on the performance of thin-film composite (TFC) membranes, Journal of Chemical and Process engineering, 1 (2014) 1-8.
[40] A. Osatiashtiani, B. Puértolas, C.C.S. Oliveira, J.C. Manayil, B. Barbero, M. Isaacs, C. Michailof, E. Heracleous, J. Pérez-Ramírez, A.F. Lee, K. Wilson, On the influence of Si:Al ratio and hierarchical porosity of FAU zeolites in solid acid catalysed esterification pretreatment of bio-oil, Biomass Conversion and Biorefinery, 7 (2017) 331-342.
[41] A.J. Kajekar, B.M. Dodamani, A.M. Isloor, Z.A. Karim, N.B. Cheer, A.F. Ismail, S.J. Shilton, Preparation and characterization of novel PSf/PVP/PANI-nanofiber nanocomposite hollow fiber ultrafiltration membranes and their possible applications for hazardous dye rejection, Desalination, 365 (2015) 117-125.
[42] H. Ravishankar, J. Christy, V. Jegatheesan, Graphene oxide (GO)-Blended polysulfone (PSf) ultrafiltration membranes for lead ion rejection, Membranes, 8 (2018) 77.
[43] M. Sarkar, S. Poddar, Studies on the Interaction of Surfactants with Cationic Dye by Absorption Spectroscopy, Journal of Colloid and Interface Science, 221 (2000) 181-185.
[44] N. Zaghbani, A. Hafiane, M. Dhahbi, Separation of methylene blue from aqueous solution by micellar enhanced ultrafiltration, Separation and Purification Technology, 55 (2007) 117-124.
[45] M. Schwarze, L. Schaefer, L. Chiappisi, M. Gradzielski, Micellar enhanced ultrafiltration (MEUF) of methylene blue with carboxylate surfactants, Separation and Purification Technology, 199 (2018) 20-26.
[46] S. Qiu, L. Wu, X. Pan, L. Zhang, H. Chen, C. Gao, Preparation and properties of functionalized carbon nanotube/PSF blend ultrafiltration membranes, Journal of Membrane Science, 342 (2009) 165-172.
[47] N. Jiang, R. Shang, S.G.J. Heijman, L.C. Rietveld, High-silica zeolites for adsorption of organic micro-pollutants in water treatment: A review, Water Research, 144 (2018) 145-161.

[48] Y.K. Ong, F.Y. Li, S.-P. Sun, B.-W. Zhao, C.-Z. Liang, T.-S. Chung, Nanofiltration hollow fiber membranes for textile wastewater treatment: Lab-scale and pilot-scale studies, Chemical Engineering Science, 114 (2014) 51-57.
[49] S. Chakraborty, B.C. Bag, S. Das Gupta, S. De, J.K. Basu, Separation and fractionation of dye solution by nanofiltration, Separation Science and Technology, 38 (2003) 219-235.
[50] S. Jana, M.K. Purkait, K. Mohanty, Removal of crystal violet by advanced oxidation and microfiltration, Applied Clay Science, 50 (2010) 337-341.
[51] S.R. Panda, S. De, Preparation, characterization and performance of ZnCl2 incorporated polysulfone (PSF)/polyethylene glycol (PEG) blend low pressure nanofiltration membranes, Desalination, 347 (2014) 52-65.
[52] Y. Zheng, G. Yao, Q. Cheng, S. Yu, M. Liu, C. Gao, Positively charged thin-film composite hollow fiber nanofiltration membrane for the removal of cationic dyes through submerged filtration, Desalination, 328 (2013) 42-50.

Graphical abstract

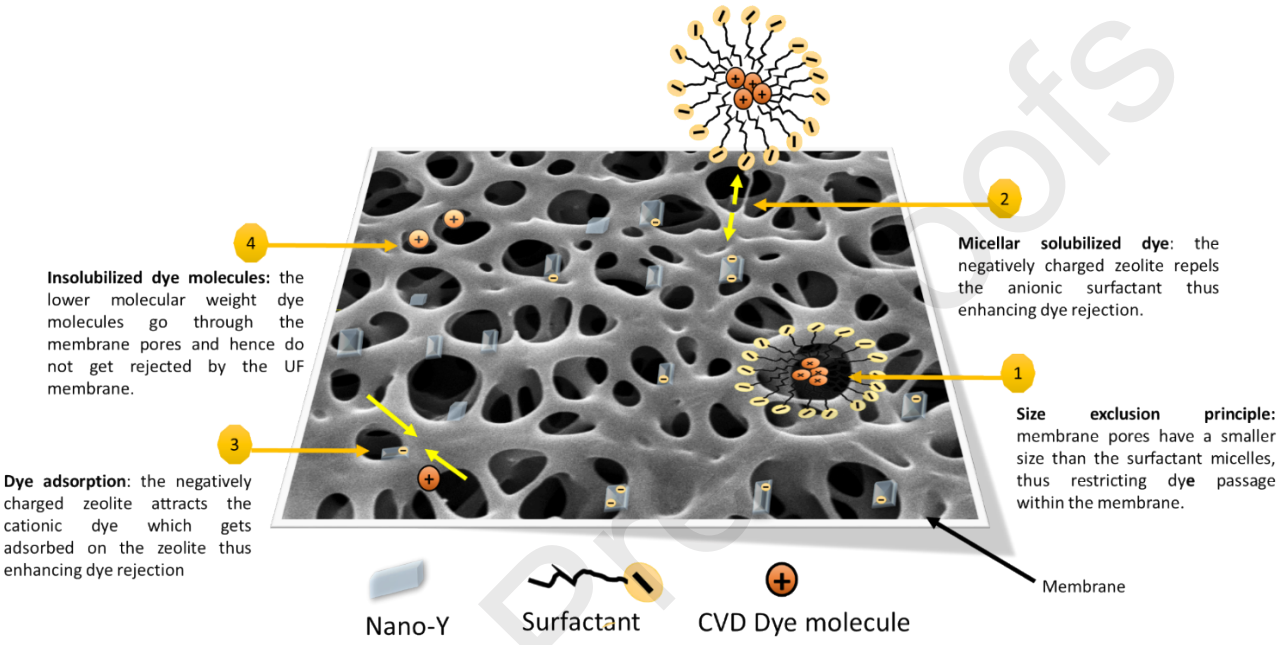

Highlights:

1. Micellar enhanced ultrafiltration for the removal of low molecular weight dye molecules
2. Nano-Y/PSf UF membranes with improved hydrophilicity
3. Uniform nano-Y distribution, with particles situated at the pore openings
4. Membranes breaking through the trade-off of selectivity and permeability with high rejection and flux

Declaration of interests

☒ The authors declare that they have no known competing financial interests or personal relationships that could have appeared to influence the work reported in this paper.

☐The authors declare the following financial interests/personal relationships which may be considered as potential competing interests: